European Journal of Wood and Wood Products (2025) 83:88
https://doi.org/10.1007/s00107-025-02245-9

ORIGINAL ARTICLE

Deformation measurement of twisted timber beam using UAV SfM photogrammetry and a new feature extraction algorithm

Juan Ortiz-Sanz[1] · Guillermo Bastos[1] · Mariluz Gil-Docampo[1]

Received: 26 July 2024 / Accepted: 7 March 2025 / Published online: 22 March 2025

Abstract
Drones facilitate the monitoring of large structures through feature extraction from point clouds generated through Structure-from-Motion photogrammetry. In the present study, we determined the deformation of a structural timber strip subjected to simultaneous bending and torsion. Three cameras were used. Two of them are pre-installed on the UAVs utilized, and the third is a consumer-grade Canon camera. All three were configured in flight mode. The geometry of the timber strip was generated through photogrammetry from the photos taken with each camera at a height of 1.5 m. The results were compared with the reference geometry, which was also created using the Canon camera on the ground at an average distance of 0.92 m. This reference geometry was previously validated in a preparatory project using extensometers with 1-µm precision. A Python-based algorithm was developed to automatically extract the position of the centroid and the rotation of each cross-sectional segment of the strip from UAV-based photogrammetric point clouds. Deformations measured by each of the three devices and the new algorithm are compared with actual deformation. The accuracy in measuring displacement and rotation of the centroid of strip cross-sections ranged between − 0.05 and 0.09 mm and between 0.00° and 0.24°, respectively.

1 Introduction

Photogrammetry is a non-invasive measurement technique that has been widely used in engineering and architecture for decades. It enables the reconstruction of accurate 3D models of objects using photographs taken from different angles, allowing for full-field measurement of distances, areas, and volumes with high accuracy (Keyvanfar and Shafaghat 2022). Moreover, it produces high-resolution and cost-effective representations of structures. Similar to laser scanning, it requires proper positioning of photographic devices (ensuring access and field of view) and may also require capturing a large number of images (Valença et al. 2017).

Using onboard cameras on unmanned aerial vehicles (UAVs) allows for the extension of photogrammetric techniques to large structures, such as civil infrastructure (Mohammadi et al. 2021; Zhao et al. 2021), slopes (Song et al. 2023), and architectural structures (Achille et al. 2015; Lara-Bocanegra et al. 2022). Pargieła (2023) conducted a bibliographic review of the techniques and conditions employed for the acquisition of measurement data using UAV-based photogrammetry. Her study highlighted the importance of enabling comparisons between results obtained under different study conditions, a principle we have followed in this work. It also confirmed that self-calibration is the most common procedure, which involves applying an algorithm that simultaneously orients the photographs and calculates the camera parameters. Self-calibration yields results comparable in quality to those obtained through pre-calibration using a well-conditioned photographic network, and precise field measurements of ground control points, which are also incorporated in this study. Congress' (2018) review included the application of close-range photogrammetry for monitoring infrastructure. The review demonstrated the improvements in speed and safety achieved in structure inspections through this technique.

Photogrammetry is particularly valuable for capturing complex geometries that are difficult to measure, such as gridshells. These structures, used in roofs and coverings, are composed of structural grids made of linear members, commonly timber strips. Being compression-only structures, they achieve efficiency by minimizing bending moments and shear forces, although variable loads can still induce bending and torsional stresses. The double-curved shape of

✉ Juan Ortiz-Sanz
juan.ortiz@usc.es

[1] Departamento de Ingeniería Agroforestal, Higher Polytechnic School, Universidade de Santiago de Compostela, Lugo, Spain

gridshells is strongly influenced by the forming process so the bending stress cannot be completely neglected. In most practical applications, obtaining the final shape analytically is not feasible (Jiang et al. 2018). Consequently, designing complex structures like gridshells can be intricate and sometimes challenging (Caffarello et al. 2022).

Measuring a prototype of a complex structure may be required to validate numerical models of deformation and structural strength, as well as to facilitate maintenance operations, thereby minimizing the risks associated with manual measurements (Ozbek et al. 2010). To this end, the extraction of features from 3D models is essential. Various methods, such as edge extraction and centerline calculation from point clouds (PCs), are used to build simplified 2D or 3D models and integrate linear elements into finite element analysis. However, limited research has explored the processing of photogrammetric PCs, which is of highly relevant because these PCs show unique characteristics compared to laser scanned PCs (Xu et al. 2017). Some of these studies can be found in the past decade, using PCs from Terrestrial Laser Scanning (TLS) (Jo et al. 2018; Gichun et al. 2019) or UAV-based Structure-from-Motion (SfM) photogrammetry (Soni et al. 2015; Chiu et al. 2017).

Recently, several authors have successfully extracted horizontal and vertical cross-sections of cylindrical concrete tanks (Siwiec and Lenda 2022; Lenda and Marmol 2023; Al-Saedi et al. 2024) by combining SfM-UAV and TLS. In these cases, the extraction of the structural faces was performed manually by intersecting the point clouds with vertical or horizontal planes. Guo et al. (2023) employed an algorithm to extract the straight centerlines of columns and the spherical centers of bolt-ball nodes (Guo et al. 2021) in long-span steel structures. However, these studies do not reflect the true deformation of the longitudinal axis or the torsion experienced by the structural element.

When the section of an element is constant, as is typically the case in structures, determining centerlines (Kresslein et al. 2018; Yeritza et al. 2022) facilitates linking geometry with numerical modeling, as centerlines can be converted into beam elements in FEM analysis (Schleicher and Herrmann 2020). Jeong et al. (2020) conducted experiments on a wooden structure with a cross-section of 4.8 m × 2.5 m and a height of 3 m. They compared measurements from a 3D model obtained through UAV-based photogrammetry with those from an electronic distance measurement device. With a flight height of 6 m and an image capture rate of 1 s, the error ranged from 6 to 28 mm. Applications for feature extraction and structural health monitoring are still in their early stage (Yang et al. 2014). In the field of element identification in PCs, Wang and Kim (2019) provided a summary of applications in the construction industry. The reconstruction of 3D models from PCs can be limited to geometric data or extended to semantic modeling, which includes object recognition.

With the aim of contributing to the measurement of complex structures, we present a study on centerline extraction and orientation determination using UAV-based Structure-from-Motion (SfM) photogrammetry to assess the deformation of a timber strip used in gridshells. The orientation is determined based on plane recognition of the face captured with the highest quality by the camera. We developed a series of Python scripts for this geometric analysis and to evaluate the achieved accuracy and precision.

Studies applying photogrammetry to capture structural deformation aim to achieve the highest possible accuracy under optimal laboratory conditions (Glaser et al. 2012; Kassotakis et al. 2021), or by combining photogrammetry with other techniques (Camarda et al. 2010; Backhaus et al. 2024). Esmaeili et al. (2019) reviewed publications on photogrammetry applied to health monitoring of large structures, but UAV-based photogrammetry was not included. In contrast, this study, although conducted indoors, employed a photographic configuration resembling flight mode to facilitate its application to larger-scale structures. The aim of the present study is to extend to full-scale structures that can be photographed in a single drone flight without using targets.

2 Materials and methods

Photogrammetry is commonly used to generate meshed 3D models of existing objects. The algorithms that extract the position from the point cloud are detailed in Sects. 2.2.2 and 2.2.4. To contribute to the aforementioned measurement of a 3D model of an existing structure, we assessed the level of detail of the photogrammetric model of a structural beam. Specifically, it is a single glulam (glued laminated timber) strip, which has been employed in gridshells. Its section measures 100 × 25 mm. It is 600 mm long, of which 510 mm were photographed. A Class I-measuring tape (European Parliament and The Council of the EU 2014) was used for scaling purposes in all the photogrammetric projects. Five Schreiber Messtechnik sensors were used: four SM222.8.1.S and one SM260.40.1.ST. They have 1 µm-precision.

The devices employed for photographing were Canon EOS 2000D with an EF 20-1:2.8 lens, DJI Phantom 4 Pro 2.0 and DJI Mavic Mini (see Fig. 1), which cost 420 €, 2000 € and 500 €, respectively. The Canon EOS series has been mounted aboard UAVs (Rau et al. 2012), and that type of UAVs is among the most representative on the commercial market (Burdziakowski 2020). The characteristics of the three cameras are listed in Table 1. The weight of the Canon camera, the Phantom drone, and the Mavic Mini drone are 475 g, 1388 g and 249 g, respectively.

Fig. 1 Photographic devices: **a** Canon EOS 2000D; **b** DJI Phantom 4 Pro v2.0; **c** Mavic Mini

Table 1 Specifications of the employed cameras

Camera	Canon EOS 2000D	DJI FC6310 (Phantom)	DJI FC 7203 (Mavic)
Sensor type	CMOS	CMOS	CMOS
Sensor (mm)	22.3 × 14.9	1″ (13.2 × 8.8)	1/2.3'' (6.17 × 4.55)
Pixels	6000 × 4000	5472 × 3648	4000 × 3000
Resolution (MP)	24	20	12
Pixel size (mm)	0.0037 × 0.0037	0.0024 × 0.024	0.0015 × 0.0015
Focal length (mm)	20	8.8	4.25
35 mm equivalent Focal distance (mm)	32.3	24	24

Ultra-wide focal lengths (< 20 mm) should generally be avoided due to significant distortion issues, though they are useful for capturing 360° scenes (Pepe and Constantino 2021). Sensor size also impacts image quality, with the 28.4 mm sensor found in most DSLR cameras delivering the best results. Smaller sensors—such as 11.0 mm in midrange cameras and 6.72 mm in compact digital cameras—tend to introduce more noise into the image (Matthews 2008).

The photos were processed to build the 3D models using Metashape v1.7.6 (Agisoft LLC 2022a). Feature extraction was carried out through Python v3.9.12 (Python Software Foundation 2020) code and the Python library PyVista v0.34.1 (The PyVista Developers 2022).Data processing was performed on a computer with 32 GB of memory, an Intel(R) Core (TM) i7-9700F CPU and an Nvidia GeForce GTX 1660 GPU.

The process carried out in each photogrammetric project consists of the following phases: scene preparation, photography, processing the photographs in Metashape to generate the 3D model, exporting the model as *ply, and processing it using Python code, which determines the position and the orientation of its wide face for each strip section.

For each of the three cameras used, the displacement of the timber strip is calculated for each coordinate as the difference between its position in the loaded state and its position in the unloaded state. The displacements obtained from each device are then compared.

2.1 Validation of ground-based photogrammetry as a reference method

To evaluate the quality of a measurement obtained through UAV photogrammetry, a first step is to establish a ground truth that allows comparing a displacement measurement using different devices (Luhmann 2010). The ground truth used is a reference method which provides sufficiently high accuracy. Typically, when capturing images using a UAV, this is done from above the object due to space constraints, with a gimbal configuration, and to avoid backlighting from below. In our case, to determine the reference position of each point on the surface of the timber strip, we chose to use tripod-based SfM photogrammetry combined with targets placed on the underside of the strip as the reference method. This approach allows the top and side faces to be visible for subsequent overhead photography sessions without physically manipulating the element.

To determine whether ground-based photogrammetry has sufficient accuracy and can be considered a reference method, it was compared to contact sensors, as illustrated in Fig. 2. The scene consists of four extensometers beneath the timber strip, uncoded targets under the strip (named

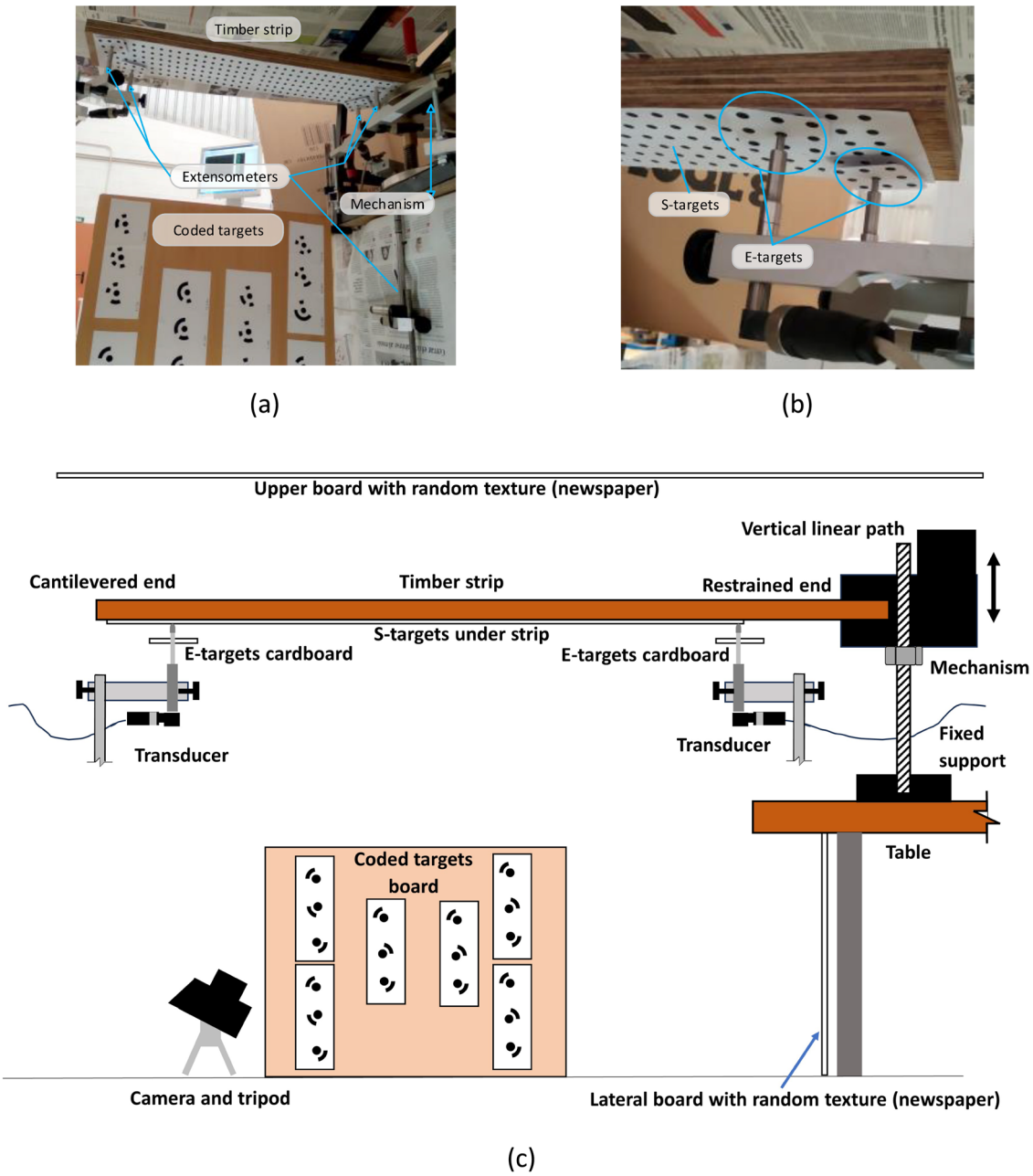

Fig. 2 **a** Setup of the comparison between photogrammetry and contact sensors; **b** Detail of the cantilevered end; **c** Schematic of the ground-based assembly

S-targets), uncoded targets attached to the movable part of the extensometers (E-targets), a fifth extensometer under the table that supports the mechanism, a panel of coded targets, and the mechanism to which the strip is constrained.

Four Schreiber Messtechnik SM222.8.1.S sensors were placed on each corner of the strip, and a fifth Schreiber Messtechnik SM260.40.1.ST sensor was placed on the table to detect a displacement of the fixed support. In Fig. 2b, two types of uncoded targets are shown: E-targets located on the mobile part of each extensometer, and S-targets, positioned on the underside of the strip. E-targets consist of a block of 8 targets, used to support the comparison between photogrammetry and sensors, based on the displacement between E-targets and the respective reading of the sensor. The average distance at which photographs were taken with the DSLR ground camera in both positions was 0.92 m (ranging between a minimum of 0.88 m and a maximum of 0.98 m), with a Ground Sampling Distance (GSD) of 0.017 mm/pixel. The S-targets consist of a total of 198 circular targets arranged in 33 rows and 6 targets per row.

The minimal radius of the central solid circle of the targets should be approximately 4–5 pixels (Agisoft LLC 2024), which means that in this case, the minimum radius of targets located 0.92 m from the sensor and perpendicular to it is 0.9 mm. A size five times larger than the minimum was chosen to ensure a sufficient safety margin for locating the most distant and tilted targets relative to the sensor. Consequently, each target had a diameter of 5.8 mm, and they were spaced 15.5 mm apart. These targets allow for evaluating the accuracy and precision along the strip.

Since the ground-based projects will serve as a reference for the UAV-based projects, the camera was always pointed toward the center of the strip. The angle formed by the camera-object line relative to the horizontal plane ranged between 36° and 47°.

To assist the photogrammetric software in recognizing points for internal and external camera orientation in each position, boards with random textures (e.g., newspapers) were placed in various locations within the scene.

Two positions were established on the mechanism. For each position, sensor readings were recorded, allowing for the determination the actual vertical displacement of the E-targets between the two established positions. If the displacement recorded by the four sensors are very close to each other, the displacements of the S-targets should also be very similar. Therefore, based on the sensors' readings, we know the actual displacement of all targets.

For each position of the mechanism, a photographic session was conducted with the Canon camera from the ground, aiming at the center of the strip. The configuration of a photogrammetric photography session heavily depends on the characteristics of the scene, such as lighting conditions, weather, shape and texture of the object, camera position and orientation, overlap between consecutive photos, and the software used. Light indirectly affects measurement quality, as it can cause photos to have blurred areas due to insufficient depth of field or motion blur. This factor is more limiting in situations where artificial light cannot be used. The camera was configured according to the instructions provided by the Metashape developer (Agisoft LLC 2022b): the ISO was set to 100, as it should be as low as possible to maximize the quality of the generated 3D model; the aperture should be high enough to achieve sharpness, with a recommended range between f/8 and f/11. The aperture was set to f/11. Given that the lighting conditions were poor but a tripod was used, the shutter speed was set to 1 s. A flash was not used, also following the developer's guidelines.

In the first and second positions 32 photos were taken. The *raw images were converted to *TIFF and loaded into the photogrammetric software.

Each photogrammetric project conducted had an image overlap of between 80 and 90%, and a very good texture pattern. Under these conditions, as indicated by the software developer, we rely on the autocalibration procedure, which means no camera lens pre-calibration is needed.

In the photogrammetric process, the 3D model was scaled and positioned using a board with 18 coded targets per side (Fig. 2), which remained fixed throughout the entire experiment. The positions of the uncoded targets on the strip were extracted from the two photogrammetric projects, and the displacements provided by photogrammetry were determined based on them. The difference between photogrammetric displacement and true displacement provides the measurement error for the 32 E-targets and 198 S-targets of ground-based photogrammetry. Next, the mean and standard deviation of the error for each type of target were calculated, providing information about the suitability of ground-based photogrammetry as a reference method.

Thus, we can assess the accuracy of multiple photogrammetry checkpoints with respect to the measurement provided by the transducers.

One of the factors that affect the measurements obtained by photogrammetry is the parameters entered during the processing of the photographs in the photogrammetric software. For this reason, this first experiment was also used to determine the optimal settings of Metashape.

The developer's instructions provide general guidelines, not specific numerical values, for these parameters. Typically, these guidelines need to be adapted to each project by testing the results with different parameter values. The core process in photogrammetry is the alignment process, which involves finding common features in photographs taken from different perspectives of the same object. "Generic preselection" aims to speed up this process by performing an initial, less precise matching between pairs of photos. With "reference preselection" in "sequential mode," it is assumed that the photographs were taken along a regular path. This means that the numerical order of the photos matches the spatial order of the camera's trajectory. Using this information, the program searches for common features between each pair of consecutive images.

The "key point limit" indicates the upper limit of feature points on each image to be taken into account during the current processing stage. Setting the value to zero allows Metashape to find as many key points as possible. The "tie point limit" indicates the upper limit of matching points for each image. Setting the value to zero does not apply any tie point filtering.

"Guided image matching" effectively boosts the number of keypoints per image as if the value of "key point limit" were straightforwardly increased, but without significant growth in processing time. For objects with flat surfaces, such as the analyzed timber strip, it helps to prevent divergence of some parameters.

We tested the following parameter settings to approach the optimal one, meaning the configuration that resulted in

the smallest errors. Each of the following configurations was tested with the same two datasets, corresponding to the two positions of the timber strip, as shown in Table 2.

2.2 Projects under flexural–torsional load

2.2.1 Setup of the scene

Once we established the Metashape settings common to all tests and verified that the reference photogrammetric projects had sufficient accuracy to be considered as such, we worked on two scenes corresponding to the unloaded and loaded states of the timber strip under a flexural–torsional load. The main task of this study is to measure the deformation between both load states, using UAV photogrammetry as the analyzed technique and ground-based photogrammetry as the reference method. The scene is shown in Fig. 3. One end of the strip was fixed. We evaluated the deformation from an unloaded to a loaded state by applying a torsional dead load to the other end: specifically, 127.5 N applied through a 1000 mm-long beam, orthogonal to the longitudinal axis of the strip. It is necessary to carry out a separate photogrammetric project for each state (unloaded and loaded) to accurately determine the displacements experienced by each particle of the timber strip.

For each load state, four photographic sessions were conducted: one from the ground (Fig. 3a) and three from the top of the beam (Fig. 3b), simulating the position of a drone flying over a structure. For the 3D model generated from these three photographic sessions, we compared the beam's centerline position and rotation with those calculated from the corresponding session on the ground, which serves as the reference truth, as previously stated.

As previously mentioned, images captured using a UAV are typically taken from above the object. To establish a common reference coordinate system for both ground-based and UAV-based projects, two small inclined panels with additional coded targets were attached to the main panel. They can be seen in Fig. 3b under the timber strip. The SfM algorithm employed by modern photogrammetry software orients overlapping images automatically, without requiring prior camera calibration (Altuntaş 2021). The ability of SfM approaches to carry out automatic camera calibration and image orientation has largely removed photogrammetric expertise as a pre-requisite for achieving straightforward models (Remondino and Fraser 2006). Thus, the purpose of the targets used in this study is not camera calibration.

The measurement quality provided by the photogrammetric technique depends, all other variables being equal, on the photographing distance: the closer the object we aim to measure, the higher the measurement quality we will obtain. In this study, the photographing distance for the UAV-based projects was set at 1.5 m, ranging between a minimum of 143 cm and a maximum of 159 cm. This distance is considered safe and realistic, given the quality of current drone positioning systems in flight. The rest of the camera settings are listed in Table 3.

The measurement quality depends on the specific configuration of each photogrammetric project, which is heavily influenced by several factors. The use of UAVs introduces additional factors to consider, such as flight altitude, UAV speed, and wind intensity (Eisenbeiss and Sauerbier 2011). In aerial photography using drones, the *shutter speed* is typically set between 1/500 and 1/1000 of a second (Radulescu and Vladareanu 2017). A lower shutter speed—i.e., a longer exposure time—than 1/500 may result in image blur due to the relative motion between the object and the UAV. The higher the shutter speed, the shorter the *exposure* time, which necessitates a higher *ISO* setting. This increase leads to greater shot noise, resulting from the random arrival of photons at the sensor (O'Connor et al. 2017). Such noise could compromise the reliability of the 3D model obtained through photogrammetry. Additionally, an aperture greater than f/8 (due to the proximity to the structure) and an ISO of 100 should be used. Each photo should be taken as perpendicular as possible to the axis of the structural elements to ensure even focus across the entire scene.

Image exposure settings (shutter speed, aperture, ISO) are highly dependent on the scene being photographed. In fact, using the lowest possible ISO helps ensure maximum image resolution. The shutter speed values shown in Table 3 were selected based on prior tests of the scene. It is recommended to use the best available camera, with a larger sensor and

Table 2 Parameters settings tested in Metashape

Configuration	A	B	C	D	E
Generic preselection		Yes	Yes	Yes	Yes
Reference preselection		Sequential	Sequential	Sequential	Sequential
Key point limit	40,000	50,000			
Key point limit per pixel					2100
Tie point limit	6000	10,000			
Guided image matching			Yes		Yes
Adaptive camera model fitting	Yes	Yes	Yes	Yes	Yes

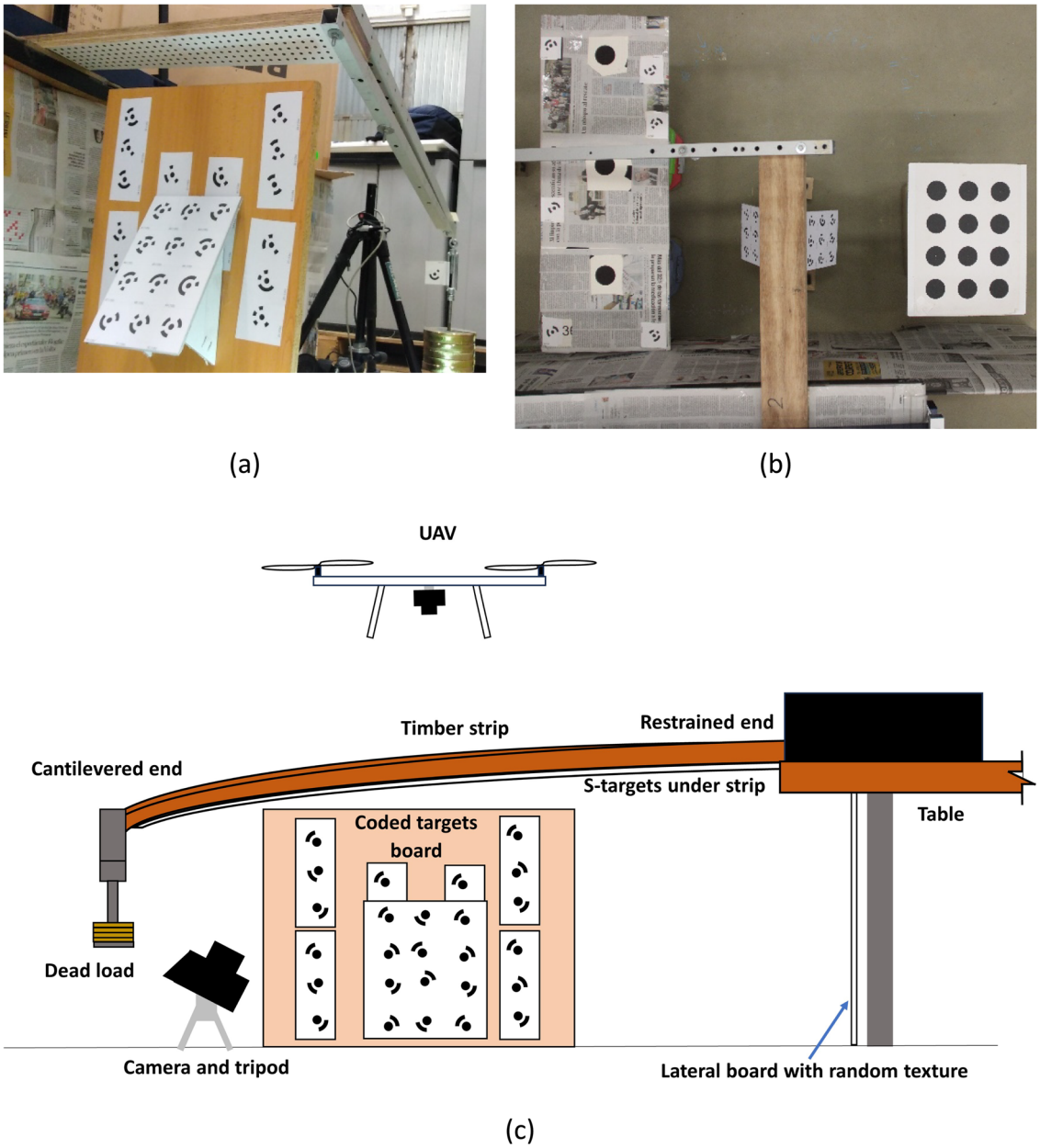

Fig. 3 Flexural–torsional experiments: **a** Scene setup during the ground-based reference project; **b** Sample photo from the UAV-based projects; **c** Schematic drawing of the loading assembly and camera positions in the ground-based and UAV-based projects. For clarity, the horizontal panels visible in **b** are omitted in **c**

resolution, that is compatible with the largest drone, and the UAV should fly at a slow speed.

The list of performed photogrammetric projects is summarized in Table 4. Two projects were carried out from the ground, to serve as the ground truth (ground-based reference projects), while six projects were conducted by photographing from above, simulating flight conditions (UAV-based projects). The objective was to measure the deformation, for each device, by comparing the loaded 3D model with the unloaded 3D model. First, the photo sessions of the unloaded cases were performed (T1, T3, T5 and T7), and then, those of the loaded cases (T2, T4, T6 and T8).

In the following sections, we explain how the displacement and rotation induced by the dead load on the cantilevered strip are computed. First, in Sect. 2.2.2, these variables are calculated using the information provided by the S-targets from the ground-based projects and the point clouds of the strip's 'adjacent faces' (AFs). Then, in Sect. 2.2.3, the computation is based on the point clouds from the UAV-based projects. Next, the error is calculated as the difference

Table 3 Settings of the used cameras

	Canon EOS 2000D		DJI FC6310 (Phantom)	DJI FC7203 (Mavic)
	Ground	Flight		
Shutter speed (s)	1	1/395	1/400	1/400
ISO	100	1600	3200	3200
Aperture	F11	F4	F5	F2.8
Average distances at which photographs were taken (m)	0.92	1.5	1.5	1.5
GSD (mm/pixel)	0.017	0.028	0.041	0.054

between the distances and angles from projects T3 to T8, and the displacements and angles calculated from the ground-based reference projects T1 and T2, for each section in relation to the previous section.

2.2.2 Ground-based reference projects

Two projects were conducted to obtain the ground truth for the UAV-based projects. This reference data was acquired using ground-based photogrammetry, with targets placed on the underside of the strip, under the same conditions as those described in the previous section. These projects used the optimal photogrammetric processing option verified in Sect. 2.1. A total of 31 photographs were taken in the unloaded state and 44 photographs in the loaded state (Fig. 3a), with an overlap between 80 and 90%. The same camera settings as in the previous section were used.

The high accuracy achieved in the reference photogrammetric projects was obtained by minimizing the photographing distance, using a tripod, and employing an artificial light source. For both the unloaded case (T1) and for the loaded case (T2), the timber strip was photographed and its 3D model was generated by Metashape. Apart from the PC, this model captured the coordinates of the S-targets under the strip. The photogrammetric network—quantity, positions and orientations of the camera—was the same as the one used in Sect. 2.1. The steps to extract the center and the orientation of the timber profile for each section are visualized in Fig. 4. The information used to calculate each section's position and rotation consists of the locations of the non-coded targets on the wide face and the point cloud from the lateral face, as shown in Fig. 4b. Each row of six targets serves as a reference for positioning each strip section.

To determine the center of each section, the first step is to calculate the fitting line for a row of points using the scikit-spatial library (Hynes 2023) of Python (see Fig. 4d). It is assumed that each section remains a planar parallelogram after the strip undergoes torsion. This fitting line intersects the fitting planes of the lateral faces (see Fig. 4b) at two points, which lie on the edges of the cross-sectional profile. Next, the two normal vectors to the wide face are calculated based on the six closest targets on each side (see Fig. 4e). Above those two vertices, the other two are located at a distance equal to the timber strip's thickness along those normal vectors. Finally, the center point is determined as the centroid of the four vertices for a given cross-section, as shown in Fig. 8. Regarding the orientation, it is represented by the normal vector to the wide face, since this is the face photographed at a more favorable angle, and thus its PC is of higher quality than those of the lateral faces. This normal is obtained by calculating the fitting plane of the row of targets of each section and the two adjacent rows (see Fig. 4c).

These operations are repeated across the 34 sections, corresponding to the 34 rows of S-targets, for the unloaded case (T1) and the loaded case (T2). The difference in the positions of the centroids and the orientations of the normals between both projects provide the ground truth variables.

2.2.3 UAV-based projects

In the same scene as in the previous section, two photogrammetric projects (unloaded and loaded) were conducted for each of the three drone-mounted systems that were evaluated: Canon EOS 2000D EF 20 1:2.8, DJI FC6310 (Phantom), and DJI FC7203 (Mavic). The horizontal panels with coded and non-coded targets on the left and right of the strip (Fig. 3b) were placed and used to scale the 3D results only for the six UAV-based projects. Notably, in the photographs taken for the UAV-based projects (Fig. 3b), the coded targets of the small inclined panels attached to the main panel are visible. A total of 81 and 88 photos were taken for the first device's projects, 70 and 82 for the two projects of the second device, and 57 and 88 for the third device studied. Again, the image overlap ranged from 80 to 90%.

For this study, the structural element was photographed from above, with the optical axis always vertical. This is

Table 4 List of photogrammetric projects

	Ground-based reference projects		UAV-based project					
Device	Canon		Canon		Phantom Pro		Mavic Mini	
	Unloaded	Loaded	Unloaded	Loaded	Unloaded	Loaded	Unloaded	Loaded
Project	T1	T2	T3	T4	T5	T6	T7	T8

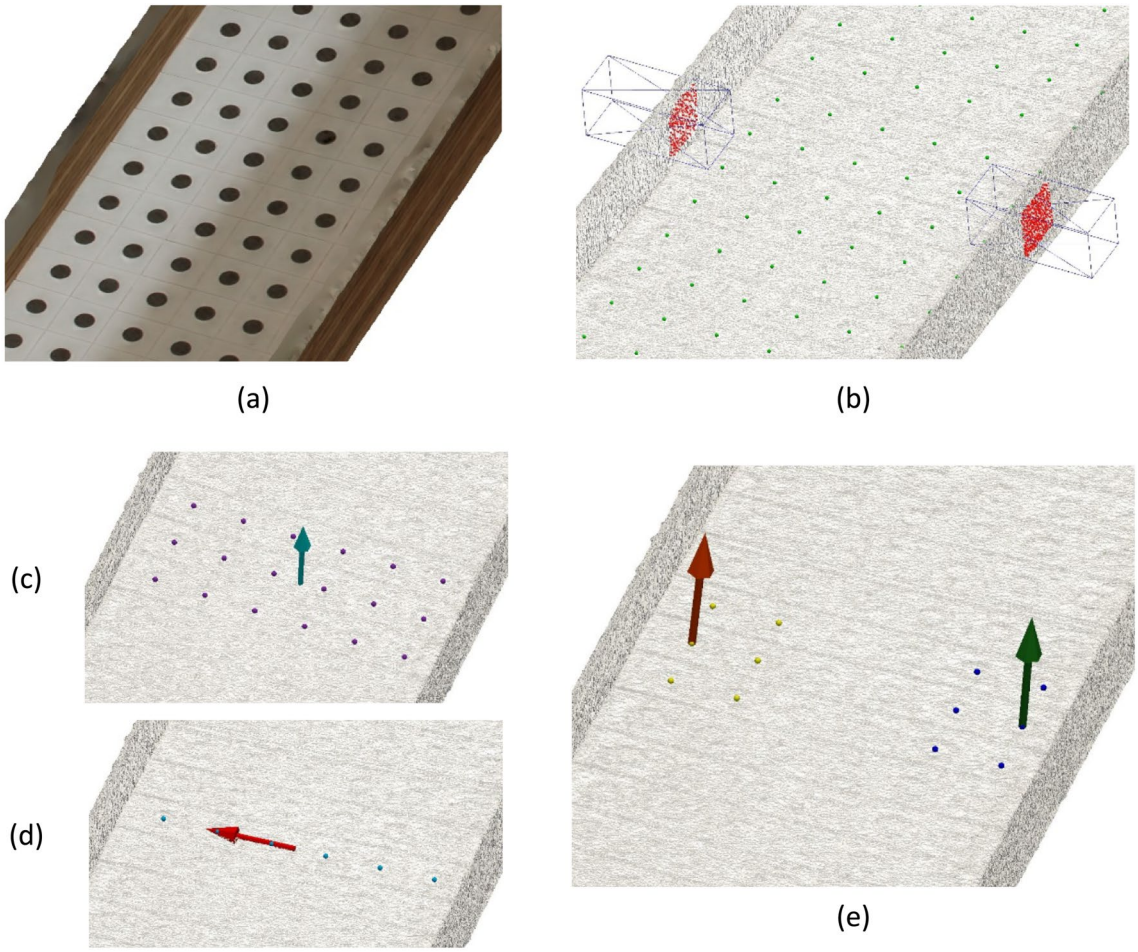

Fig. 4 T1 and T2: **a** Textured view of the 3D model; **b** Targets' locations and PCs of the lateral faces; **c** Points considered in a single section to determine the face's orientation; **d** Row of points in a section; **e** Normal direction of the wide face on both sides

the most challenging configuration, as it requires camera translation and rotation to properly capture both side faces in addition to the top face. The angle formed by the camera-object line relative to the horizontal plane ranged between 62° and 90°. As previously explained, we chose a camera-to-object distance of 1.5 m. The camera settings were adjusted to simulate flight mode.

To model a surface, it must be photographed from various points around it. In addition to changing the camera position, it is also advisable to vary the optical axis to ensure it is orthogonal to the object. To ensure the applicability of this technique to full-scale structures, we maintained the unfavorable condition of keeping the optical axis always vertical. We photographed along a rectangular horizontal grid, ensuring that the photos had a 90% overlap in both directions: parallel and perpendicular to the timber strip. Most of the photos fully captured the entire top face of the strip. An overview of the scene is shown in Fig. 3b.

The position of each of the 34 sections of the timber strip is determined differently compared to the ground-based projects T1 and T2. Instead of using the target locations obtained in those projects (Fig. 4a), the point cloud generated from the object's surface based on UAV photographs (Fig. 5a) was used. Metashape, like any photogrammetric software, provides the meshed 3D model. The point cloud used corresponds to the vertices of that mesh.

For each section on this PC, its position along the timber strip was determined by aligning the point cloud with points from ground-based reference projects. The timber strip's centerline position and each section's angle were computed by identifying points on three faces arranged on a plane as perpendicular as possible to the strip's centerline. From now on, the face fully visible to the UAV camera will be called the "top face" (TF), in contrast to the AFs, which are captured from a highly unfavorable optical axis angle. The algorithm for extracting the centerline follows these steps:

(A) Seed point selection

This is the only manual task: a point is selected on the TF. This point is chosen using the mouse on the

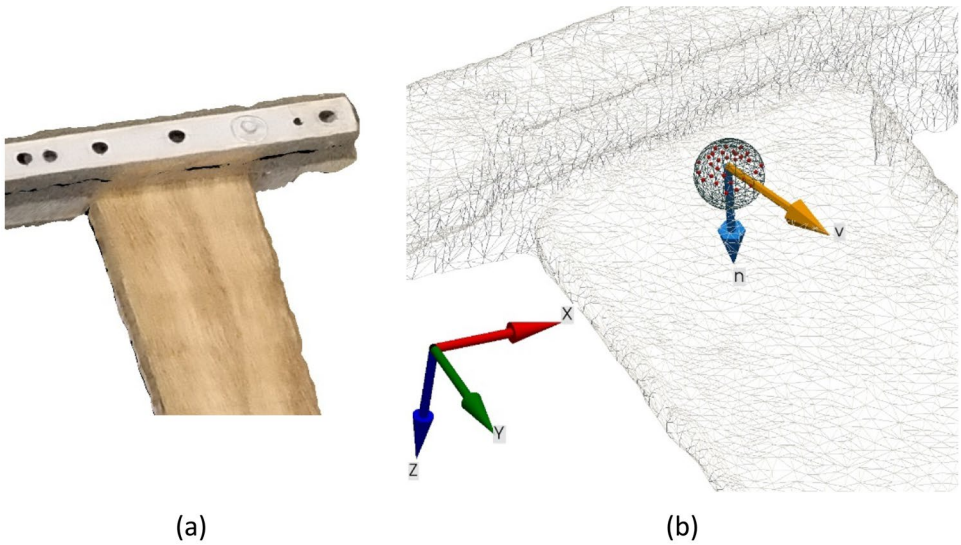

Fig. 5 Algorithm start in projects T3 to T8: **a** Textured model; **b** LF normal vector $\vec{n}$ and LF parallel vector $\vec{v}$ (PyVista)

mesh display of PyVista. To enable the comparison of the feature extraction on the eight projects, the initial seed point was defined in each project so that it had the same distance to the aluminum beam at the cantilevered end (see Fig. 4a).

As illustrated in Fig. 5, after selecting this point, a sphere centered on it is created, and the points contained within the sphere are selected. The fitting plane for these points is then determined using the SVD algorithm: the *fit_plane_to_points* function of PyVista returns the center and the normal $\vec{n}$ of this plane. To identify the points corresponding to the lateral faces, the process begins by adding a second vector $\vec{v}$, whose direction is randomly chosen within the plane orthogonal to $\vec{v}$.

As observed in Fig. 5b, the longitudinal axis of the timber element was initially aligned with the global Y-axis. The results will be presented considering the global coordinate system.

(B) Strip profile recognition

The point corresponding to the centerline and the orientation of the TF are determined for each section of the profile. To do this, a third vector $\vec{t} = \vec{n} \times \vec{v}$ is introduced. These three vectors are used as a local coordinate system. The goal is for $\vec{v}$ to be oriented orthogonally to the lateral faces, so that $\vec{t}$ becomes tangent to the centerline. This local reference system is iteratively reoriented using the points found on the three faces. At the end of the orientation process, the centroid of the profile and the orientation of the TF are recorded.

Each orientation process begins by assigning $\vec{v}$ the direction orthogonal to the AFs and estimating the first preliminary centroid. The process starts by detecting TF points within a box that moves in steps, adapting to a twisted surface. A sample case is displayed in Fig. 6.

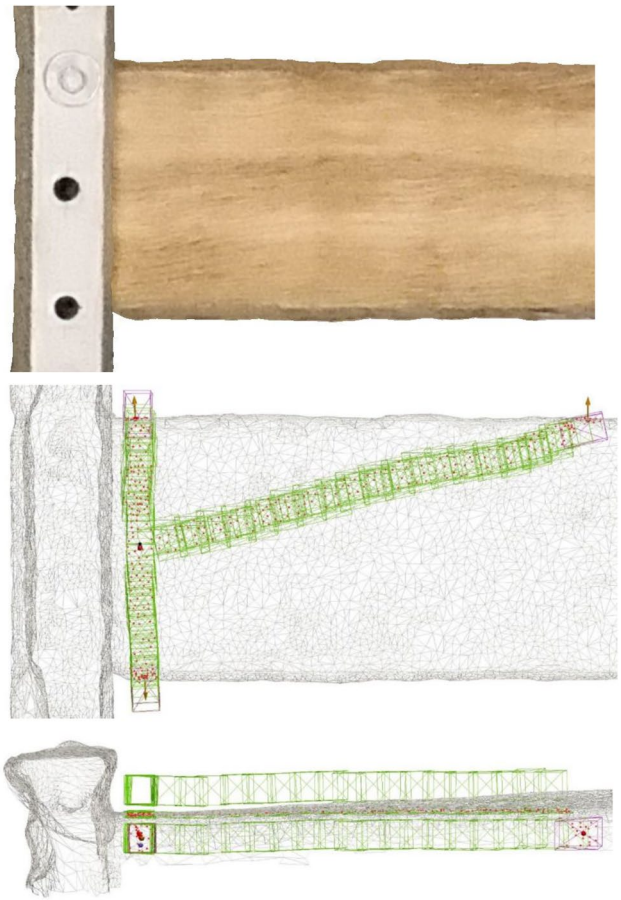

Fig. 6 Top view and front view of the preliminary centroid

At each step, points belonging to the AFs are searched for within different boxes along $\vec{v}$. When points are found on any AF, the normal vector and point defining their fitting plane are calculated. Then, $\vec{v}$ is assigned the

direction of the normal. The process is repeated along the $+\vec{v}$ and the $-\vec{v}$ directions until the variation in the $\vec{v}$ direction falls below a threshold value. The position of the initial centroid is then calculated as the midpoint between the fitting planes of both Afs in the $\vec{v}$ direction, at a distance from the TF equal to half the thickness of the timber strip.

(C) Centerline extraction

Next, the aforementioned operations are repeated on the next section, creating a new preliminary centroid by incrementing the position of the last recorded centroid by 15 mm along $\vec{t}$, as this is the distance between rows of uncoded targets.

For the points of the PC detected in each section, the objective is for $\vec{n}$ to be orthogonal to the TF, and $\vec{v}$ to be orthogonal to the AFs. Thus, a centroid C, along with the intrinsic coordinate axes $\vec{n}$, $\vec{v}$ and $\vec{t}$ can be used as a reference to define the ideal rectangular cross-sectional profile of the strip, as shown in Fig. 7: the centering operations aim to reduce the distance between the points of the 3D model and the ideal faces of the profile.

The centerline extraction starts by loading the preliminary center C and vectors $\vec{n}$ and $\vec{v}$ from the previous step. Then, C is displaced iteratively along $\vec{n}$ while the distance between the points and the ideal face plane decreases. As this distance decreases, the displacements continue in smaller steps by applying a factor of 0.25 until the displacement falls below a threshold value of 1 µm.

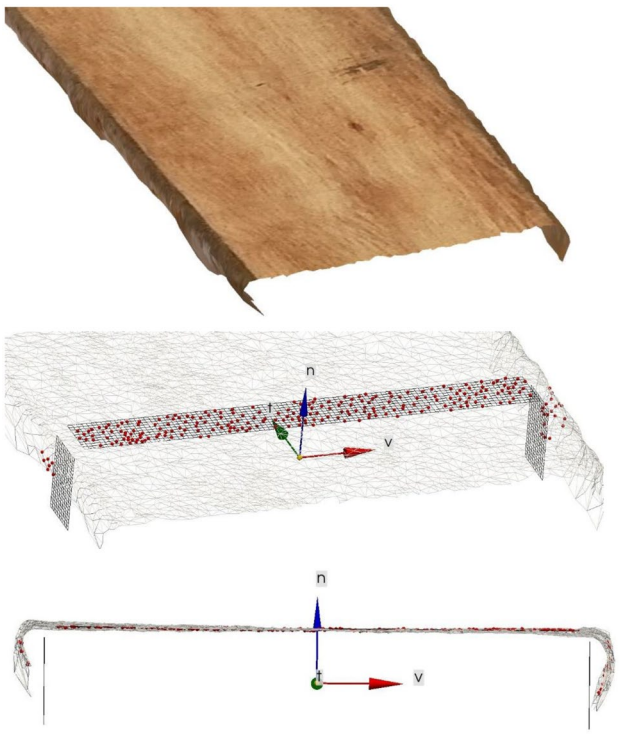

Fig. 7 Position of the ideal section within the actual 3D model of a sample section

As shown in Fig. 7, centering along the Afs in the $\vec{v}$ direction is a more challenging operation, as the modeled points of the AFs are limited and dispersed due to occupying few pixels in the photographs. First, to find the AFs' points, the detection is performed on the TF along the $+\vec{v}$ and $-\vec{v}$ directions, as in step B. Based on the farthest point from C, a new detection box is launched in the expected position of the Afs. Given the unrealistic curved shape of the AFs (see Fig. 7), only the farthest points from C are selected. More precisely, the distance between C and each point is calculated. Then, the retained points are those whose distance from the center lies between the maximum distance and 0.3 times the standard deviation below the maximum distance. If no AFs' points are found, the farthest point of the TF will be kept as the only AF point.

The fitting plane of each AF is calculated if at least 4 points are available. Otherwise, the centroid of the retained points is computed, but $\vec{v}$ is adopted as the normal of the AF. Then, the intersection points of the planes of these AFs' and the ray $\{\vec{v}, C\}$ are determined. C is then placed at the midpoint between both AFs, with this displacement constrained to the cross-sectional plane $\{\vec{n}, \vec{v}\}$. The direction of $\vec{v}$ is updated to align with the normals of the AFs if they form an angle of less than 4° with $\vec{v}$.

The normal vector is calculated based on the PC from the TF. The rotation of each profile section is represented by the rotation of this normal vector.

In summary, for all 34 sections of the timber beam, we compare the geometric precision between flight projects and ground projects for three variables: the X- and Z-coordinates of the centerline, and the orientation of the TF. For each device, the variation in each geometric variable from the unloaded to the loaded case is measured. The difference in these measurements between each device and the reference cases constitutes the error. Finally, basic statistical analysis is performed on these errors.

3 Results and discussion

3.1 Validation of ground-based photogrammetry as a reference method

The results of these configurations were analyzed in two groups: S-targets and E-targets (see Fig. 2b). The findings are summarized in Table 5.

Table 5 Error analysis of targets' locations

Configuration		S-targets	E-targets
A	μ (mm)	0.219	0.226
	σ (mm)	0.048	0.292
B	μ (mm)	0.015	0.004
	σ (mm)	0.482	0.283
C	μ (mm)	0.004	− 0.039
	σ (mm)	0.068	0.249
D	μ (mm)	− 0.084	− 0.055
	σ (mm)	0.084	0.335
E	μ (mm)	0.293	0.288
	σ (mm)	0.084	0.321

We adopted the settings of C for the other eight projects, as it clearly outperformed the others in terms of both average error and standard deviation: the average error was 1/229,500 for the S-targets and 1/23,530 for the E-targets, relative to the average camera-to-object distance of 918 mm. These values demonstrate the high measurement quality of SfM photogrammetry for determining the positions of points marked with targets.

3.2 Projects under flexural–torsional load

The centerline of the reference project T2 is shown in Fig. 8. It can be observed that hidden areas are partially extrapolated in Metashape, with 'extra material' added around the farthest edges, one of the adjacent faces being completely hidden from the camera.

Despite the inaccuracies in modeling, a smooth centerline is reconstructed from the 34 cross-sections of the reference projects. The displacement of these cross-sections, i.e., the difference between the coordinates of T2 and T1, is presented in Fig. 9a. Small fluctuations of up to 0.3 mm are observed in the last sections of the strip along the X-coordinate (cross-sections from 25 to 35). This may be attributed to the strip's roughness, as its sides are composed of adhered wood laminates, as shown in Fig. 10. The angle rotated due to the load is depicted in Fig. 9b.

This uniformity in the centerlines of T1 and T2, along with the results from the previous section, validates their use as reference projects. Consequently, we can proceed with the comparison of the other projects against this reference.

In Fig. 11, the results of T8 are presented. The AFs were captured at an angle of less than 30° between the optical axis and the object surface. Consequently, the generated PCs

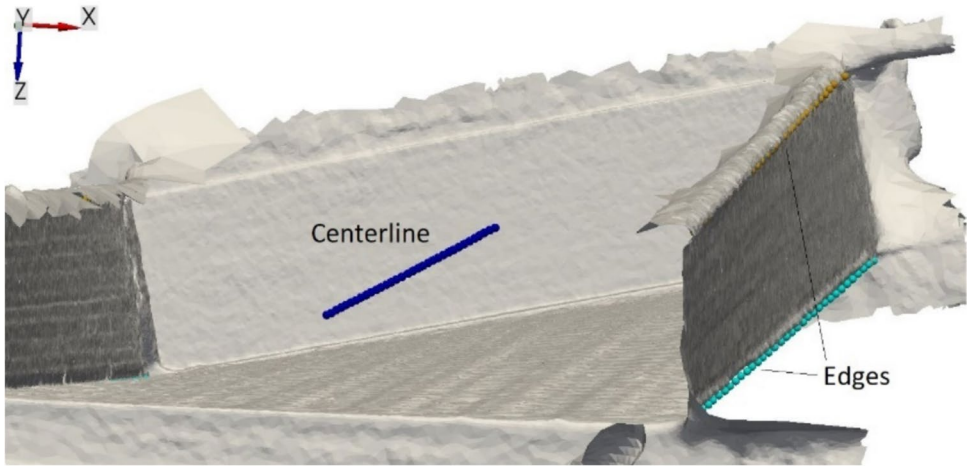

Fig. 8 Overview of the centerline extraction in project T2 (Canon camera positioned at ground level) based on the S-targets in 34 determined cross-sections

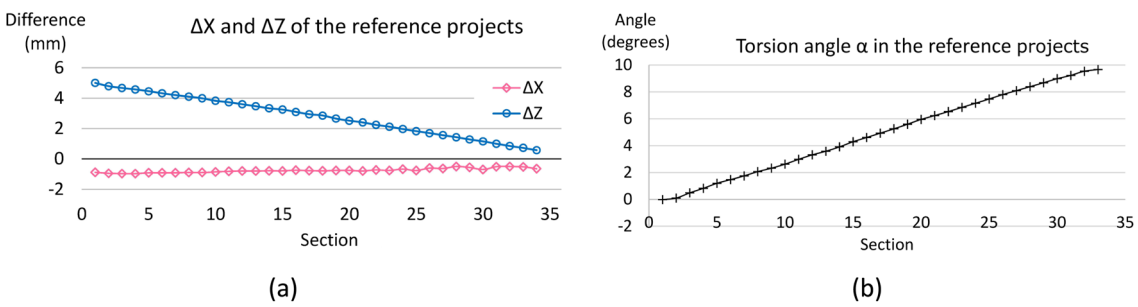

Fig. 9 Displacement **a** and rotation angle **b** in T2 relative to T1

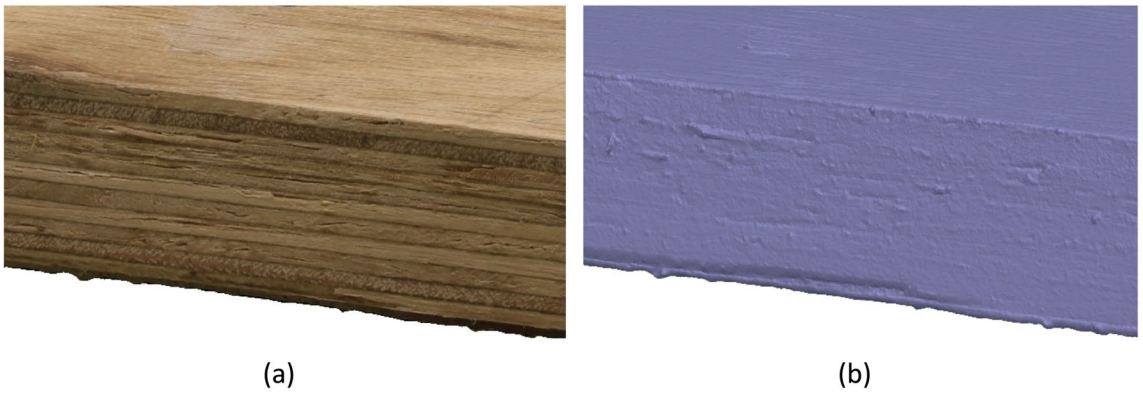

Fig. 10 High-precision photogrammetric model of the strip at a 200 mm distance: **a** Textured view; **b** Shaded view

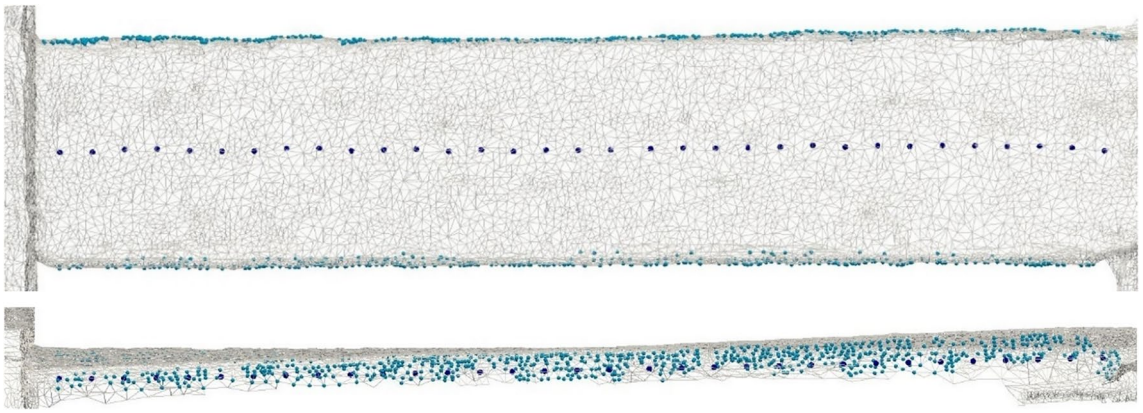

Fig. 11 Overview of the centerline extraction in project T8 using the Mavic Mini

contain very few points on these side faces, which represents the primary challenge in the entire process. Furthermore, the surface of the AF is more irregular, affecting the centroid locations along the direction of $\vec{v}$, which is roughly aligned with the global X-axis.

The error in the X displacement is presented in Fig. 12, while the error in the Z displacement is shown in Fig. 13. As an example, in the case of the error in the X-coordinate using the Phantom, the error results from calculating $(X_{T6} - X_{T5}) - (X_{T2} - X_{T1})$, where, for example, X_{T6} refers to the X-coordinate of the points on the centerline of the timber strip determined from the photogrammetric project T6. The deviation along the X-axis is on the order of millimeters, as anticipated from Fig. 11. Conversely, the deviation along the Z-axis is an order of magnitude smaller than that of the X-axis. This highlights the critical importance of ensuring that the modeled faces occupy a sufficient portion of the photographs to reliably identify the cross-section of the structural element.

Table 6 presents the basic statistics of the center positions, aimed at estimating the accuracy of obtaining the centerline of a full-scale structure. These values correspond to the displacement induced by the load in projects T3 to T8, relative to the same variables in the reference projects T1 and T2.

The last measurement extracted from the PCs of the projects was the rotation angle due to the flexural–torsional load, which was based on the normal vector $\vec{n}$ of the TF (see Fig. 7). The error for each strip section is displayed in Fig. 14, and the corresponding statistics are summarized in Table 7. In the detection of rotation, a greater difference is observed between the UAVs: the Phantom Pro camera outperformed that of the Mavic Mini, even more so than in the error in the Z-coordinate. This suggests that the Mavic Mini yields a less precise, i.e., more disperse PC for the TF.

An advantage of photogrammetry is highlighted in Tables 6 and 7: the uniformity of the quality of the generated model. The PC of the modeled timber strip exhibited bumps on the order of 5 mm. Despite this, the uniformity of the PC contributes to high accuracy (mean value of error) and precision (standard deviation of error) in the extracted displacements and angles. The Phantom Pro

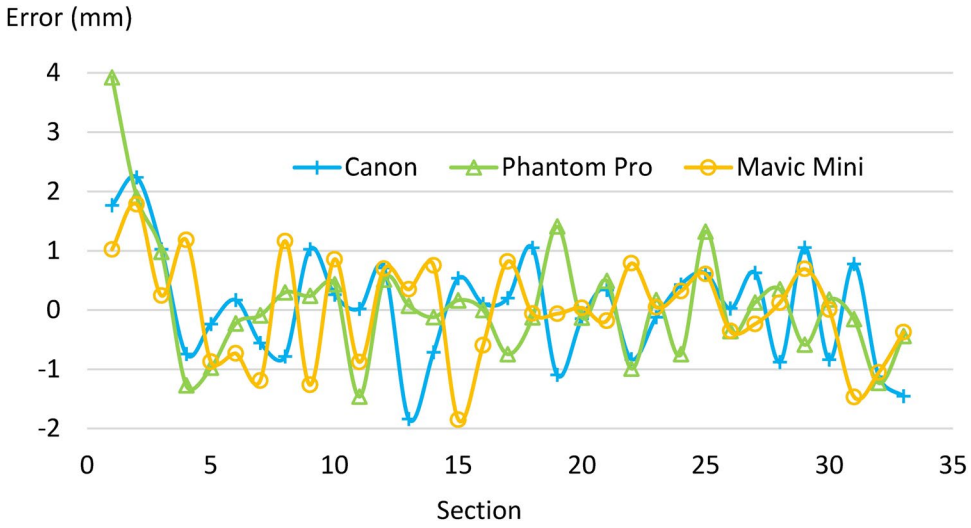

Fig. 12 Error in the X coordinate of the centerline

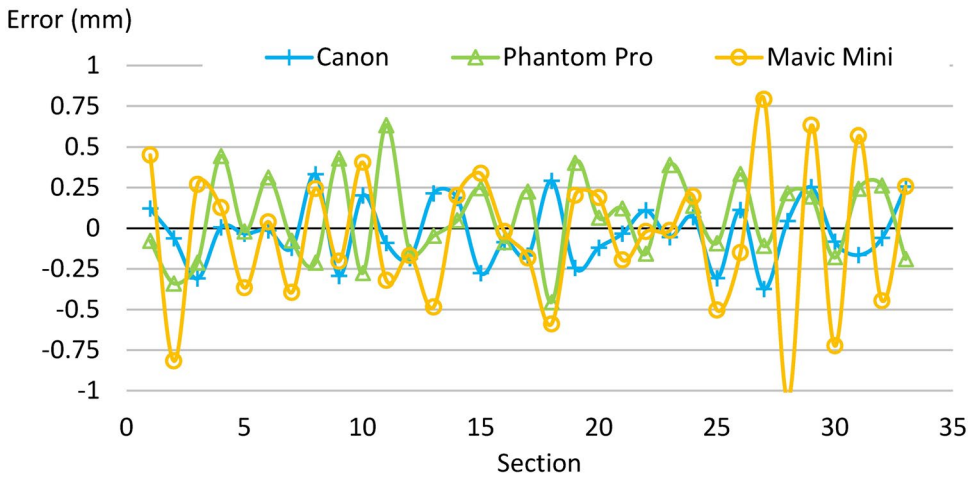

Fig. 13 Error in the Z coordinate of the centerline

Table 6 Statistics of error in displacements detection compared to the reference projects

	X-coordinate			Z-coordinate		
	Canon	Phantom Pro	Mavic Mini	Canon	Phantom Pro	Mavic Mini
Mean value (mm)	0.05	0.09	0.01	− 0.03	0.06	− 0.05
SD (mm)	0.92	1.02	0.86	0.19	0.26	0.43
Minimum value (mm)	− 1.84	− 1.46	− 1.85	− 0.37	− 0.46	− 1.06
Maximum value (mm)	2.24	3.92	1.79	0.33	0.63	0.79

achieved slightly lower precision and accuracy than the Mavic Mini in capturing the less visible AFs. The opposite occurred when capturing the clearly visible TF: the Mavic Mini showed greater dispersion in the PC, which was also observed in the rotation angle. In all cases, the Canon camera achieved better results than the UAVs, suggesting that mounting a consumer-grade or professional-grade camera on an UAV could be considered to achieve high-quality models.

4 Future work and full-scale structures

Although the PCs were of low quality, they were sufficient to achieve sub-millimetric accuracy in locating the structural element's centerline. The factor that most limited the cloud quality was the camera-to-object distance; for example, as shown in Fig. 10b, at a distance of 0.2 m the resulting model even captures sub-millimetric 3D details

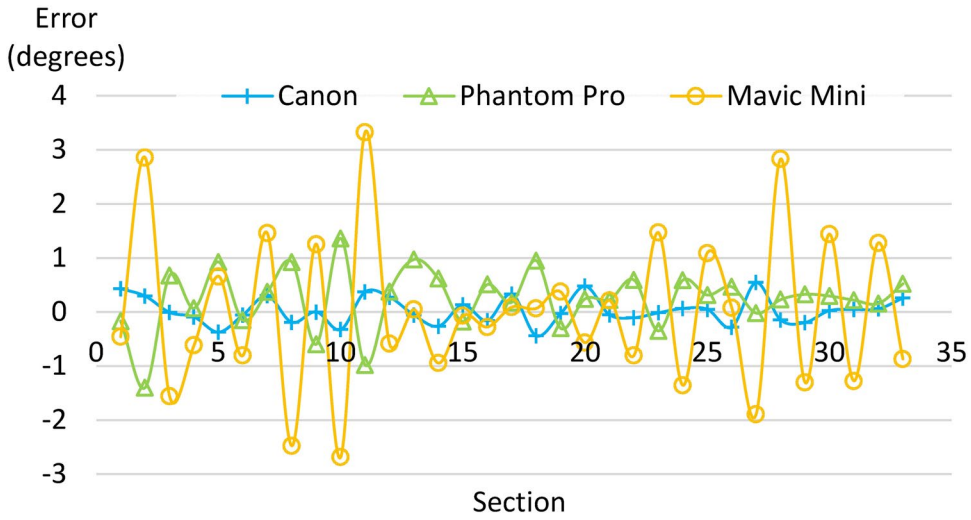

Fig. 14 Error in the rotation angle α

Table 7 Statistics of error in the rotation angle compared to the reference projects

	Rotation angle (degrees)		
	Canon	Phantom Pro	Mavic Mini
Mean value (degrees)	0.03	0.24	0.00
SD (degrees)	0.25	0.56	1.45
Minimum value (degrees)	− 0.43	− 1.40	− 2.68
Maximum value (degrees)	0.54	1.36	3.32

of the object's surface. Therefore, the natural wood texture is suitable for photogrammetric modeling.

Texture is the factor that determines the applicability of this technique to other materials. A homogeneous surface lacking texture is not suitable for photogrammetry—examples include polished metal, painted surfaces, and plastic coatings. Without a heterogeneous texture, photogrammetric software cannot identify corresponding points in two or more images.

Photogrammetry has been extensively studied on concrete structures (Dai et al. 2014), where it is common to use targets—even on on-site structures (Jáuregui et al. 2003). One issue worth investigating is under what conditions a concrete surface is suitable for photogrammetry without targets. A newly cured structure exhibits a homogeneous surface, but over time it becomes more heterogeneous, as observed in the inspection of older structures.

The presented results suggest the next step: applying this method to a full-scale wood structure without using targets on the structure, using a drone with an integrated camera. Building on the gridshell case, the algorithm would need to be extended to consider the presence of fastening elements and the intersections between the timber strips. A possible approach to the problem would be to first detect the presence of an intersection and then continue searching for points of the structural element while skipping the theoretical space occupied by the intersection, extrapolating the element's centerline.

It should be remembered that, in the present work, each cross-section of a strip has been positioned individually, leading to small fluctuations in the position of each section. When applying this to a real structure, where the curvature of the elements (if present) is regular, the centroids could be averaged using a spline, which could further reduce measurement errors.

To achieve optimal results, a dense point cloud with high measurement quality is required, which necessitates a high GSD. In UAV-SfM projects, it is advisable to photograph as close as possible to the structure without compromising drone safety and while flying at a slow speed. The best available camera is also recommended, featuring a larger sensor and higher resolution, compatible with the largest drone. Lighting conditions should allow for an f/8 aperture with shutter speeds between 1/250 and 1/500, preferably at ISO 100. Flight planning should ensure that the optical axis during capture is as perpendicular as possible to the axis of the structural element, with overlaps exceeding 60%. Although this results in a large number of photographs, it is not problematic, as photogrammetric software—when properly configured—is capable of automatically processing thousands of images. In any case, photogrammetry settings will also depend on the texture, lighting, sections, and arrangement of the structural elements whose deformations are to be analyzed.

5 Conclusion

To achieve optimal results in structural health monitoring projects using UAV-based SfM photogrammetry and feature extraction, it is essential to obtain a dense point

cloud with high measurement quality, which requires a high GSD. It is advisable to capture images as close as possible to the structure—without compromising drone safety and while flying at a slow speed. The best available camera is also recommended, featuring a larger sensor and higher resolution and being compatible with larger drones. Lighting conditions should allow for an f/8 aperture, shutter speeds between 1/250 and 1/500, and preferably ISO 100. Flight planning must ensure that the optical axis during capture is as perpendicular as possible to the structural element's axis, with image overlaps exceeding 60%. Although this results in a large number of photographs, it is not problematic, as properly configured photogrammetric software can automatically process thousands of images.

In this study, the photogrammetric modeling of a timber strip was tested under simulated UAV operating conditions. Three UAV cameras were evaluated. Additionally, two new semi-automatic, Python-based feature extraction algorithms were developed to determine both positional changes along the centerline and rotations of the transverse sections of the timber strip when subjected to a combined flexural–torsional load.

Although the study was conducted in a laboratory, the photographing distance and camera settings simulated real-world conditions. As a result, the point clouds obtained in the photogrammetric projects simulating flight conditions were highly irregular. Nevertheless, knowing the actual cross-section of the timber strip allowed for highly accurate location extraction.

An average accuracy of 0.05 mm in displacements along the longitudinal axis and 0.03° in rotations of the transverse sections was achieved using a GSD of 0.028 mm/pixel. This was accomplished by photographing perpendicularly to the object from a distance of 1.5 m, with an overlap between 80 and 90%, ISO 1600, f/4, and a shutter speed of 1/395 s, using a consumer-grade digital camera commonly employed in SfM-UAV, along with the new Python-based feature extraction algorithm.

This result quality suggests the feasibility of UAV-based methods for measuring full-scale timber structures, where sub-millimeter accuracy would be sufficient to validate numerical form-finding models.

Acknowledgements This work is part of the R&D&I Project PID2020-112954RA-I00 funded by MICIU/AEI/10.13039/501100011033. This work was made possible also due to the Spanish State Research Agency (AEI), since Dr. Bastos was contracted in the framework of the postdoctoral grant Juan de la Cierva – Formación (FJC2019-039743-I/AEI/10.13039/501100011033). We thank also the regional government of Galicia (Xunta de Galicia, Spain) for the Grant "Financial aid for the consolidation and structure of competitive units of investigation in the universities of the University Galician System (2020-22)" [ED431B 2020/25].

Author contributions JOS: Conceptualization, Methodology, Investigation, Writing—Review and Editing. GB: Writing—Original Draft, Software, Investigation, Formal analysis, Visualization. MGD: Writing—Review and Editing, Supervision.

Funding Open Access funding provided thanks to the CRUE-CSIC agreement with Springer Nature. J.O.S. received research support in the frame of Grant PID2020-112954RA-I00 funded by MICIU/AEI/10.13039/501100011033, and M.G.D. from the aforementioned grant from the Xunta de Galicia (Ref. ED431B 2020/25).

Data availability No datasets were generated or analysed during the current study.

Declarations

Conflict of interest The authors declare no competing interests.

References

Achille C, Adami A, Chiarini S et al (2015) UAV-based photogrammetry and integrated technologies for architectural applications—methodological strategies for the after-quake survey of vertical structures in Mantua (Italy). Sensors 15:15520–15539

Agisoft LLC (2022a) Agisoft metashape. https://www.agisoft.com/. Accessed 2 Jul 2021

Agisoft LLC (2022b) Agisoft Helpdesk Portal—General image capture tips. In: https://agisoft.freshdesk.com/support/solutions/articles/31000149337-general-image-capture-tips. Accessed 13 Jul 2021

Agisoft LLC (2024) Agisoft Helpdesk Portal—Coded targets and scale bars. In: https://agisoft.freshdesk.com/support/solutions/articles/31000148855. Accessed 16 Sep 2021

Al-Saedi ASJ, Abed FM, Alwan IA (2024) Tank deformation analysis by combining laser scanning and photogrammetry. Eng Technol J 42:1417–1434. https://doi.org/10.30684/etj.2024.153203.1810

Altuntaş C (2021) Camera self-calibration by using SfM based dense matching for close-range images. Euras J Sci Eng Technol 2:69–82

Backhaus J, De Arriba López V, Maboudi M et al (2024) Combining UAV-based photogrammetry and structured light scanning to support the structural health monitoring of concrete structures. e-J Nondestruct Test. https://doi.org/10.5828/29797

Burdziakowski P (2020) Increasing the geometrical and interpretation quality of unmanned aerial vehicle photogrammetry products using super-resolution algorithms. Remote Sens (Basel) 12

Caffarello FM, Mascia NT, Basaglia CD, Soriano J (2022) Structural analysis of timber gridshell covered by OSB panels considering the effect of wind. J Civ Eng Arch. https://doi.org/10.17265/1934-7359/2022.06.001

Camarda M, Guarnieri A, Milan N, Vettore A (2010) Health monitoring of complex structure using TLS and photogrammetry. International archives of photogrammetry, remote sensing and spatial information sciences, vol XXXVIII, Part 5. ISPRS, Newcastle upon Tyne, pp 125–129

Chiu WK, Ong WH, Kuen T, Courtney F (2017) Large structures monitoring using Unmanned Aerial Vehicles. Procedia Eng 188:415–423. https://doi.org/10.1016/j.proeng.2017.04.503

Congress SSC (2018) Novel infrastructure monitoring using multi-faceted unmanned aerial vehicle systems—close range photogrammetry (UAV-CRP) data analysis. Civil Engineering Dissertations, p 367

Dai F, Feng Y, Hough R (2014) Photogrammetric error sources and impacts on modeling and surveying in construction engineering applications. Vis Eng 2:2. https://doi.org/10.1186/2213-7459-2-2

European Parliament and The Council of the EU (2014) Directive 2014/32/EU of the European Parliament and of the Council of 26 February 2014 on the harmonisation of the laws of the Member States relating to the making available on the market of measuring instruments (recast)

Eisenbeiss H, Sauerbier M (2011) Investigation of UAV systems and flight modes for photogrammetric applications. Photogramm Record 26:400–421. https://doi.org/10.1111/j.1477-9730.2011.00657.x

Esmaeili F, Ebadi H, Mohammadzade A, Saadatseresht M (2019) Evaluation of close-range photogrammetric technique for deformation monitoring of large-scale structures: a review. ISSGE 8:41–55

Gichun C, Seunghee P, Taekeun O (2019) A Terrestrial LiDAR-based detection of shape deformation for maintenance of bridge structures. J Constr Eng Manag 145:04019075. https://doi.org/10.1061/(ASCE)CO.1943-7862.0001701

Glaser R, Caccese V, Shahinpoor M (2012) Shape monitoring of a beam structure from measured strain or curvature. Exp Mech 52:591–606. https://doi.org/10.1007/s11340-011-9523-y

Guo M, Sun M, Pan D et al (2021) High-precision detection method for large and complex steel structures based on global registration algorithm and automatic point cloud generation. Measurement 172:108765. https://doi.org/10.1016/j.measurement.2020.108765

Guo M, Sun M, Pan D et al (2023) High-precision deformation analysis of yingxian wooden pagoda based on UAV image and terrestrial LiDAR point cloud. Herit Sci 11:1. https://doi.org/10.1186/s40494-022-00833-z

Hynes A (2023) scikit-spatial: Spatial objects and computations based on NumPy arrays. https://scikit-spatial.readthedocs.io. Accessed 5 Mar 2023

Jáuregui DV, White KR, Woodward CB, Leitch KR (2003) Noncontact photogrammetric measurement of vertical bridge deflection. J Bridg Eng 8:212–222. https://doi.org/10.1061/(ASCE)1084-0702(2003)8:4(212)

Jeong GY, Nguyen TN, Tran DK, Hoang TBH (2020) Applying unmanned aerial vehicle photogrammetry for measuring dimension of structural elements in traditional timber building. Measurement 153:107386. https://doi.org/10.1016/j.measurement.2019.107386

Jiang Y, Zegard T, Baker WF, Paulino GH (2018) Form-finding of grid-shells using the ground structure and potential energy methods: a comparative study and assessment. Struct Multidiscip Optim 57:1187–1211. https://doi.org/10.1007/s00158-017-1804-3

Jo HC, Kim J, Lee K et al (2018) Non-contact strain measurement for laterally loaded steel plate using LiDAR point cloud displacement data. Sens Actuators A Phys 283:362–374. https://doi.org/10.1016/j.sna.2018.09.012

Kassotakis N, Sarhosis V, Peppa MV, Mills J (2021) Quantifying the effect of geometric uncertainty on the structural behaviour of arches developed from direct measurement and Structure-from-Motion (SfM) photogrammetry. Eng Struct 230:111710. https://doi.org/10.1016/j.engstruct.2020.111710

Keyvanfar A, Shafaghat A (2022) Emerging dimensions of unmanned aerial vehicle's (UAV) 3D reconstruction modeling and photogrammetry in Architecture and construction management. ACE Arch City Environ. https://doi.org/10.5821/ace.16.48.10492

Kresslein J, Haghighi P, Park J et al (2018) Automated cross-sectional shape recovery of 3D branching structures from point cloud. J Comput des Eng 5:368–378. https://doi.org/10.1016/j.jcde.2017.11.010

Lara-Bocanegra AJ, Majano-Majano A, Ortiz J, Guaita M (2022) Structural analysis and form-finding of triaxial elastic timber gridshells considering interlayer slips: numerical modelling and full-scale test. Appl Sci 12

Lenda G, Marmol U (2023) Integration of high-precision UAV laser scanning and terrestrial scanning measurements for determining the shape of a water tower. Measurement 218:113178. https://doi.org/10.1016/j.measurement.2023.113178

Luhmann T (2010) Close range photogrammetry for industrial applications. ISPRS J Photogramm Remote Sens 65:558–569. https://doi.org/10.1016/j.isprsjprs.2010.06.003

Matthews NA (2008) Aerial and close-range photogrammetric technology: Providing resource documentation, interpretation, and preservation. Technical Note 428. U.S. Department of the Interior, Bureau of Land Management, National Operations Center, Denver, Colorado, p 42

Mohammadi M, Rashidi M, Mousavi V et al (2021) Quality evaluation of digital twins generated based on UAV photogrammetry and TLS: bridge case study. Remote Sens (Basel) 13:3499

O'Connor J, Smith MJ, James MR (2017) Cameras and settings for aerial surveys in the geosciences: optimising image data. Progress Phys Geogr Earth Environ 41:325–344. https://doi.org/10.1177/0309133317703092

Ozbek M, Rixen DJ, Erne O, Sanow G (2010) Feasibility of monitoring large wind turbines using photogrammetry. Energy 35:4802–4811. https://doi.org/10.1016/j.energy.2010.09.008

Pargieła K (2023) Optimising UAV data acquisition and processing for photogrammetry: a review. Geomat Environ Eng 17:29–59. https://doi.org/10.7494/geom.2023.17.3.29

Pepe M, Constantino D (2021) Techniques, tools, platforms and algorithms in close range photogrammetry in building 3D model and 2D representation of objects and complex architectures. Comput Aid des Appl 18:42–65

Python Software Foundation (2020) python. https://www.python.org/. Accessed 1 Oct 2020

Radulescu M, Vladareanu V (2017) Aerial photography and the use of photo cameras attached to drones. Sci Res Educ Air Force 19:201–206. https://doi.org/10.19062/2247-3173.2017.19.1.22

Rau JY, Jhan JP, Lo CF, Lin YS (2012) Landslide mapping using imagery acquired by a fixed-wing UAV. Int Arch Photogramm Remote Sens Spatial Inf Sci XXXVIII-1/:195–200. https://doi.org/10.5194/isprsarchives-XXXVIII-1-C22-195-2011

Remondino F, Fraser C (2006) Digital camera calibration methods: considerations and comparisons. Int Arch Photogramm Remote Sens Spatial Inf Sci 36:266–272

Schleicher S, Herrmann M (2020) Constructing hybrid gridshells using bending-active formwork. Int J Space Struct 35:80–89. https://doi.org/10.1177/0956059920924189

Siwiec J, Lenda G (2022) Integration of terrestrial laser scanning and structure from motion for the assessment of industrial chimney geometry. Measurement 199:111404. https://doi.org/10.1016/j.measurement.2022.111404

Song CR, Wood RL, Bekele B et al (2023) A Comparison of surface deformation measurement methods for slopes. Appl Sci 13

Soni A, Robson S, Gleeson B (2015) Structural monitoring for the rail industry using conventional survey, laser scanning and

photogrammetry. Appl Geomat 7:123–138. https://doi.org/10.1007/s12518-015-0156-1

The PyVista Developers (2022) PyVista. https://docs.pyvista.org/index.html. Accessed 6 Jun 2022

Valença J, Puente I, Júlio E et al (2017) Assessment of cracks on concrete bridges using image processing supported by laser scanning survey. Constr Build Mater 146:668–678. https://doi.org/10.1016/j.conbuildmat.2017.04.096

Wang Q, Kim M-K (2019) Applications of 3D point cloud data in the construction industry: a fifteen-year review from 2004 to 2018. Adv Eng Inform 39:306–319. https://doi.org/10.1016/j.aei.2019.02.007

Xu Y, Tuttas S, Hoegner L, Stilla U (2017) Geometric primitive extraction from point clouds of construction sites using VGS. IEEE Geosci Remote Sens Lett 14:424–428. https://doi.org/10.1109/LGRS.2017.2647816

Yang H, Xu X, Neumann I (2014) The Benefit of 3D Laser Scanning Technology in the feneration and calibration of FEM models for health assessment of concrete structures. Sensors 14:21889–21904

Yeritza P-P, Mani G-F, Khaled E-R (2022) Automatic 3D modeling of structural and mechanical components from point clouds. Construct Res Congress 2018:501–511

Zhao S, Kang F, Li J, Ma C (2021) Structural health monitoring and inspection of dams based on UAV photogrammetry with image 3D reconstruction. Autom Constr 130:103832. https://doi.org/10.1016/j.autcon.2021.103832